

# Resolving the location of small intracontinental earthquakes using Open Access seismic and geodetic data: lessons from the 2017 January 18 $m_b$ 4.3, Ténéré, Niger, earthquake

Timothy J. Craig<sup>1</sup> and Steven J. Gibbons<sup>2</sup>

<sup>1</sup>COMET, School of Earth and Environment, The University of Leeds, Leeds LS2 9JT, UK. E-mail: [t.j.craig@leeds.ac.uk](mailto:t.j.craig@leeds.ac.uk)

<sup>2</sup>NGI, Sognsveien 72, N-0855 Oslo, Norway

Accepted 2202 April 12 in original form 2021 December 6

## SUMMARY

A low-magnitude earthquake was recorded on 2017 January 18, in the Ténéré desert in northern Niger. This intraplate region is exceptionally sparsely covered with seismic stations and the closest open seismic station, G.TAM in Algeria at a distance of approximately 600 km, was unusually and unfortunately not operational at the time of the event. Body-wave magnitude estimates range from  $m_b$  4.2 to  $m_b$  4.7 and both seismic location and magnitude constraints are dominated by stations at teleseismic distances. The seismic constraints are strengthened considerably by array stations of the International Monitoring System for verifying compliance with the Comprehensive Nuclear Test-Ban-Treaty. This event, with magnitude relevant to low-yield nuclear tests, provides a valuable validation of the detection and location procedure for small land-based seismic disturbances at significant distances. For seismologists not in the CTBT system, the event is problematic as data from many of the key stations are not openly available. We examine the uncertainty in published routinely determined epicentres by performing multiple Bayesloc location estimates with published arrival times considering both all published arrival times and those from open stations only. This location exercise confirms lateral lateral uncertainties in seismologically derived location no smaller than 10 km. Coherence for interferometric synthetic aperture radar in this region is exceptionally high, and allows us to confidently detect a displacement of the order 6 mm in the time frame containing the earthquake, consistent with the seismic location estimates, and with a lateral length scale consistent with an earthquake of this size, allowing location constraint to within one rupture length ( $\leq 5$  km)—significantly reducing the lateral uncertainty compared with relying on seismological data only. Combining Open Access-only seismological and geodetic data, we precisely constrain the source location, and conclude that this earthquake likely had a shallow source. We then discuss potential ways to continue the integration of geodetic data in the calibration of seismological earthquake location.

**Key words:** Satellite geodesy; Earthquake hazards; Earthquake monitoring and test-ban treaty verification; Earthquake source observations; Seismicity and tectonics.

## 1 INTRODUCTION

On the 2017 January 18, a small-magnitude earthquake occurred in the Ténéré desert of northern Niger (Fig. 1a). Located at the northern edge of the Sahel, bordering the Sahara, and roughly half-way between the coasts of West Africa and the Red Sea, the source region is deep in the interior of Africa, far from any major population centres—the nearest city being Agadez,  $\sim 400$  km away. The region is similarly remote from a tectonic perspective—the nearest active plate boundaries are in northern Morocco ( $\sim 2000$  km), the Gulf of Suez ( $\sim 2400$  km) and the East Africa Rift System

( $\geq 3000$  km). The nearest instrumentally recorded earthquake to the 2017 event, of any magnitude, in the combined catalogues of Bulletin of the International Seismological Centre (ISC Bulletin hereafter; ISC 2021), is a similarly remote  $m_b$  4.5 earthquake in the southern Ahaggar mountains of Algeria,  $\sim 600$  km away. Within  $15^\circ$  ( $\sim 1650$  km) of the Ténéré earthquake, there are only 625 earthquakes reported in the full ISC Bulletin, of any magnitude.

As a result of the tectonic quiescence and remoteness of the region, Ténéré is one of the least well seismologically instrumented continental regions on Earth, with the nearest seismic station located

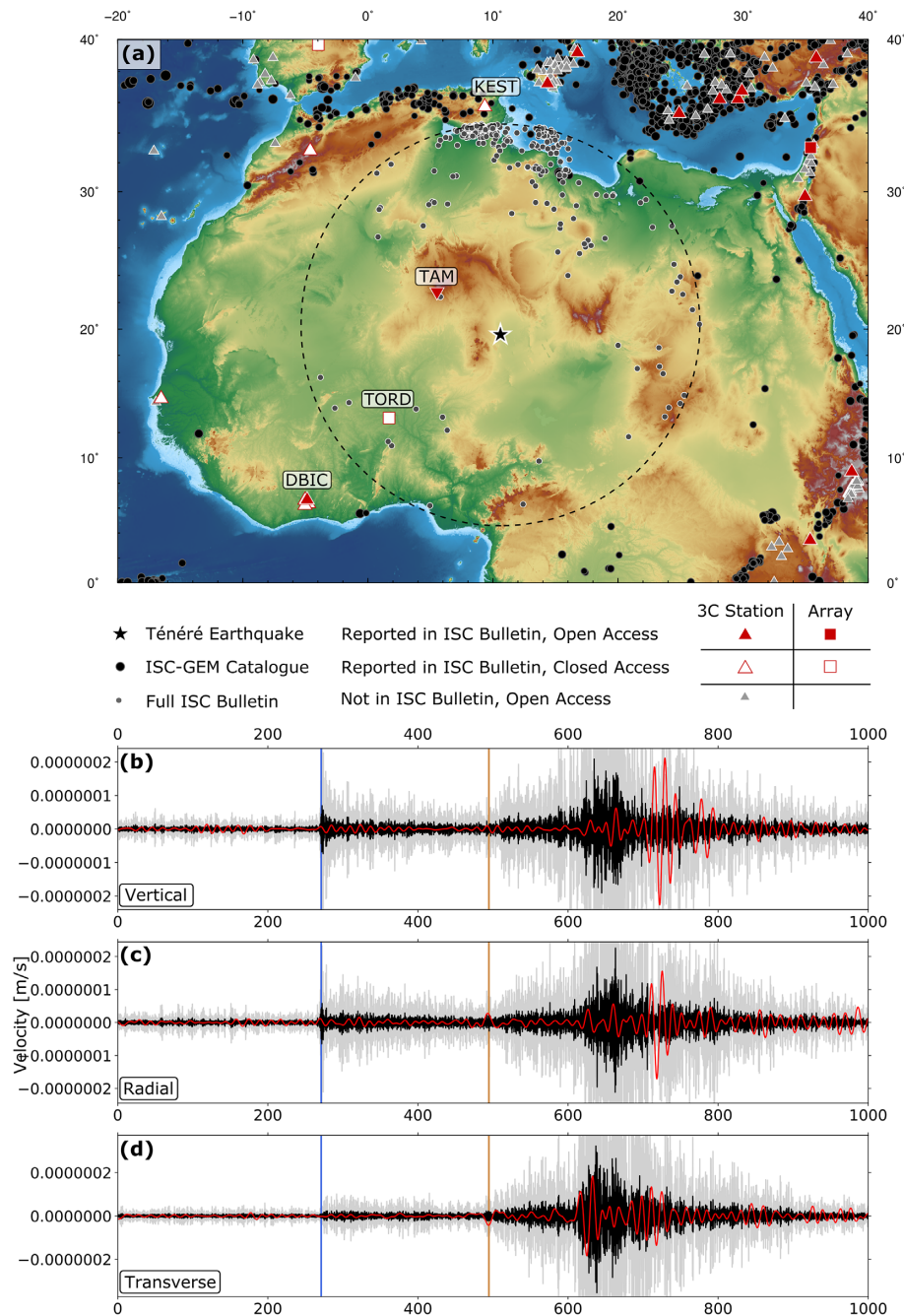


**Figure 1.** (a) Regional map, showing the 2017 Ténéré earthquake and distribution of observing seismometers. Red filled symbols indicate stations reported in the ISC Bulletin that are Open Access, white-filled symbols are those reported in the ISC Bulletin that are closed, grey are those Open Access three-component stations not reported in the ISC Bulletin. Inverted red triangle shows the location of the seismometer at Tamanrasset (Algeria), usually reporting to the ISC Bulletin, but inoperative at the time of the 2017 Ténéré earthquake. Black circles show all earthquakes in the ISC-GEM catalogue. Grey circles show every earthquake recorded in the full ISC Bulletin within  $15^\circ$  of the 2017 Ténéré earthquake. (b) Vertical component waveform from DBIC (location shown in a). Black trace is filtered between 1.0 and 4.0 Hz, red between 0.02 and 0.08 Hz, to isolate surface wave arrivals, grey is the same as black, with the amplitude scaled by a factor of 5 to emphasize the body-wave arrivals. Blue and green bars show the predicted P and S arrival times. (c) as in (b), but showing the radial component waveform. (d) as in (b), but showing the transverse component waveform.

over 600 km away (at Tamanrasset, southern Algeria—which was in fact inoperative at the time of this earthquake), and no other stations within 1000 km. For small-magnitude earthquakes, data from seismic networks at local and regional distances is crucial for the robust and accurate determination of the earthquake location (e.g. Bondár *et al.* 2004). In the absence of such data, the 2017 Ténéré earthquake offers an opportunity to test the resolving power

of global seismic networks, and the limitations of seismological location routines in the absence of near-field data. With the lack of vegetation, and the lack of major agricultural or industrial activity in the area, the Ténéré desert is also a region where the coherence of interferometric synthetic aperture radar (InSAR) images is high, enabling the detection of small-magnitude surface displacements, and we thus also aim to test how satellite geodesy can complement

seismological approaches in the location of small earthquakes in remote continental areas.

Routine seismological catalogues determined the location ( $\sim 19.6^\circ\text{N}$ ,  $10.6^\circ\text{E}$ ), and magnitude ( $m_b$  4.2–4.7) of this earthquake (see Table 1). The reported magnitude of this earthquake places it in the range of interest for low-yield nuclear tests (e.g. Barker *et al.* 1998; Chun *et al.* 2011). For such events, routine seismological monitoring is supplemented by the observational capabilities of the International Monitoring System (IMS), under the auspices of the Comprehensive Test Ban Treaty Organisation (CTBTO), most particularly through a global network of small-aperture seismic arrays and high-quality three-component seismometers. However, data from many of these networks remain subject to access restrictions, and are not currently freely available to the scientific community. This study probes how far events like the Ténéré earthquake can be studied and characterized in detail using only freely available Open Access data, and tests how reliant the location of such earthquakes is on closed-access data. We combine remote seismological and geodetic analysis to assess the validity with which routine processing approaches were able to determine the location of this earthquake. We highlight a number of issues that may cause problems for the location of rare small earthquakes in remote continental interiors, and demonstrate how the combination of careful seismological analysis with modern geodetic data can mitigate such problems, allowing the high-resolution characterization of such events.

## 2 OVERVIEW OF THE SEISMOLOGICAL OBSERVATIONS

Fig. 1 displays the source region of the 2017 January 18 earthquake together with the locations of events in the ISC GEM catalogue (ISC-GEM 2021, unrestricted) and the ISC Bulletin (limited to those within  $15^\circ$ ), and the locations of seismic stations used to constrain the location in the bulletins listed in Table 1. The map in panel (a) confirms both the absence of significant seismic events in an almost continental-scale region surrounding the epicentre and the sparsity of stations at local, regional, or far-regional distances contributing to the location estimates. Of those stations at far-regional distances (a term usually referring to distances between  $10^\circ$  and  $20^\circ$ ) only the three-component station GT.DBIC in the Ivory Coast is open for public access. Panels (b), (c) and (d) of Fig. 1 show the signal on GT.DBIC both in a high-frequency bandpass (1–4 Hz) and the lower frequency band from 12.5 to 50.0 s period. The short-period band signals are typical of far-regional continental propagation with high-frequency  $Pn$  and  $Sn$  arrivals followed by high-amplitude and slightly lower period  $Lg$  waves which dominate the wavetrain. Both  $Pn$  and  $Sn$  arrivals are followed by long codas with high-frequency energy. Both body and surface waves are visible in the longer period signal although the  $Pn$  and  $Sn$  arrivals have low signal-to-noise ratio (SNR). Only the  $Pn$  arrival is particularly useful for location purposes; the  $Sn$  arrival is extremely emergent and picking an accurate signal onset is difficult. In addition, even if the  $Pn$  arrival time can be read accurately, the distance range for this station is associated with an exceptionally large uncertainty in the modelled traveltime (e.g. Myers *et al.* 2015). The primary value of the DBIC signal is in the estimation of magnitude and the hypothesis that the event is relatively shallow in order to explain the dominant  $Lg$  and surface waves.

Fig. 2 provides both a representative selection of the available teleseismic waveforms and an overview of the global station coverage, again differentiating between stations open to the general

public and those limited to authorized parties in the CTBT system. For a seismic event with significant continental landmass in all directions within distances of  $100^\circ$  (i.e. where you would anticipate observing  $P$  waves) there is an exceptional degree of asymmetry to the observing seismic network. We have examined significant numbers of open waveforms at stations not included in the ISC bulletin, but where data are openly available (see Fig. 1a), and found in very few cases signals which both offered a high SNR and a useful location, covering an azimuthal or distance gap relative to the network displayed in Fig. 2. The best signals are found on stations to the North East; in Eastern Europe and Central Asia—a distribution that will be the result of both the network coverage, and the orientation of the focal mechanism and resultant radiation pattern (note that the focal mechanism for this earthquake is unknown). Fig. 2 shows signals on the vertical components of three 3-component stations, and (vertical component) array beams on three array stations.

Of the waveforms shown on Fig. 2, the Makanchi array (MKAR) is a 9-site primary IMS seismic array in Kazakhstan, the Mount Meron array (MMAI) is a 16-site auxiliary IMS seismic array in Israel, and the Bukovina array (BURAR) is a non-IMS 9-element array in Romania. The data from all of these arrays are openly available; MKAR and BURAR are available via the IRIS Data Management Center and MMAI is available via the GEOFON data centre at GFZ Potsdam. Each of these arrays has an aperture of only a few kilometres, with the intention that short period signals (e.g. 1–4 Hz) are coherent between sensors and that the SNR of signal arrivals can be improved by delay-and-stack beamforming (e.g. Rost & Thomas 2009). Similarly, estimating the coherence or relative power of beams in different directions allows us to estimate the backazimuth and apparent velocity of incoming wave fronts. This assists in algorithms to associate detections and helps to build confidence that a given signal detection is indeed associated with our event hypothesis, on the basis of directional coherence of arrivals.

For each array in Fig. 2, the top panel shows the array beam constructed using the predicted backazimuth and  $P$ -wave slowness, based on the ISC location. Beneath each of the array beams is a scan of backazimuth as a function of time (for a fixed apparent velocity based on the expected earthquake epicentre) and a scan of apparent velocity as a function of time (for a fixed value of the backazimuth based on the expected earthquake epicentre). These plots are a variant on the VESPA process (Davies *et al.* 1971) and allow us to confirm that each of the signals at the time of the predicted  $P$  arrival is associated with a coherent wave packet with a direction consistent with the origin hypothesis. Gibbons *et al.* (2016) performed such analysis on several array stations for an earthquake of similar magnitude near the Northern tip of Novaya Zemlya in the Russian Arctic and found double bursts of coherent energy with a delay of just over 3 s at stations at different azimuths from the epicentre. This observation supported a hypothesis of teleseismic  $pP$  phases which helped to constrain the event depth. There is no such unambiguous evidence of depth phases in the array analysis in Fig. 2. BURAR and MMAI show very little coherent energy in the coda following the initial arrival; MKAR shows coherent energy with appropriate propagation parameters far into the coda.

The remaining three panels of Fig. 2 show signals for the  $P$  arrivals at arbitrarily chosen teleseismic three-component stations (in Czechia, Saudi Arabia and Kenya). We note that the SNR for the signals at many of these stations is relatively poor, and that improvement through stack-and-delay is not possible for non-array stations. The waveforms shown in Fig. 2 also highlight the potential subjectivity in identifying the onset of a particular phase arrival, with the majority of arrivals being emergent, especially in terms

**Table 1.** Routine catalogue locations for the 2017 January 18 Ténéré earthquake together with 95 per cent confidence ellipses specified with (Smaj/Smin/Az) where Smaj and Smin are the lengths of the major and minor axes in km.

| Catalogue | Origin time (UTC) | Lat (°) | Lon (°) | Dep (km) | (Smaj/Smin/Az)   | $m_b$ |
|-----------|-------------------|---------|---------|----------|------------------|-------|
| IDC       | 21:48:19.39       | 19.5947 | 10.6106 | 0.0*     | (16.0/12.7/120°) | 4.2   |
| ISC       | 21:48:21.08       | 19.5847 | 10.6018 | 10.0*    | (10.6/7.6/125°)  | 4.3   |
| NEIC      | 21:48:22.14       | 19.6049 | 10.6491 | 10.0*    | (16.0/12.7/120°) | 4.6   |
| ISC-EHB   | 21:48:21.08       | 19.5530 | 10.7380 | 10.0*    | (7.1/5.6/117°)   | —     |
| EMSC      | 21:48:21.80       | 19.48   | 10.75   | 10.0*    | (18.5/14.9/93°)  | 4.7   |

\*Depths were fixed *a priori* during location determination.

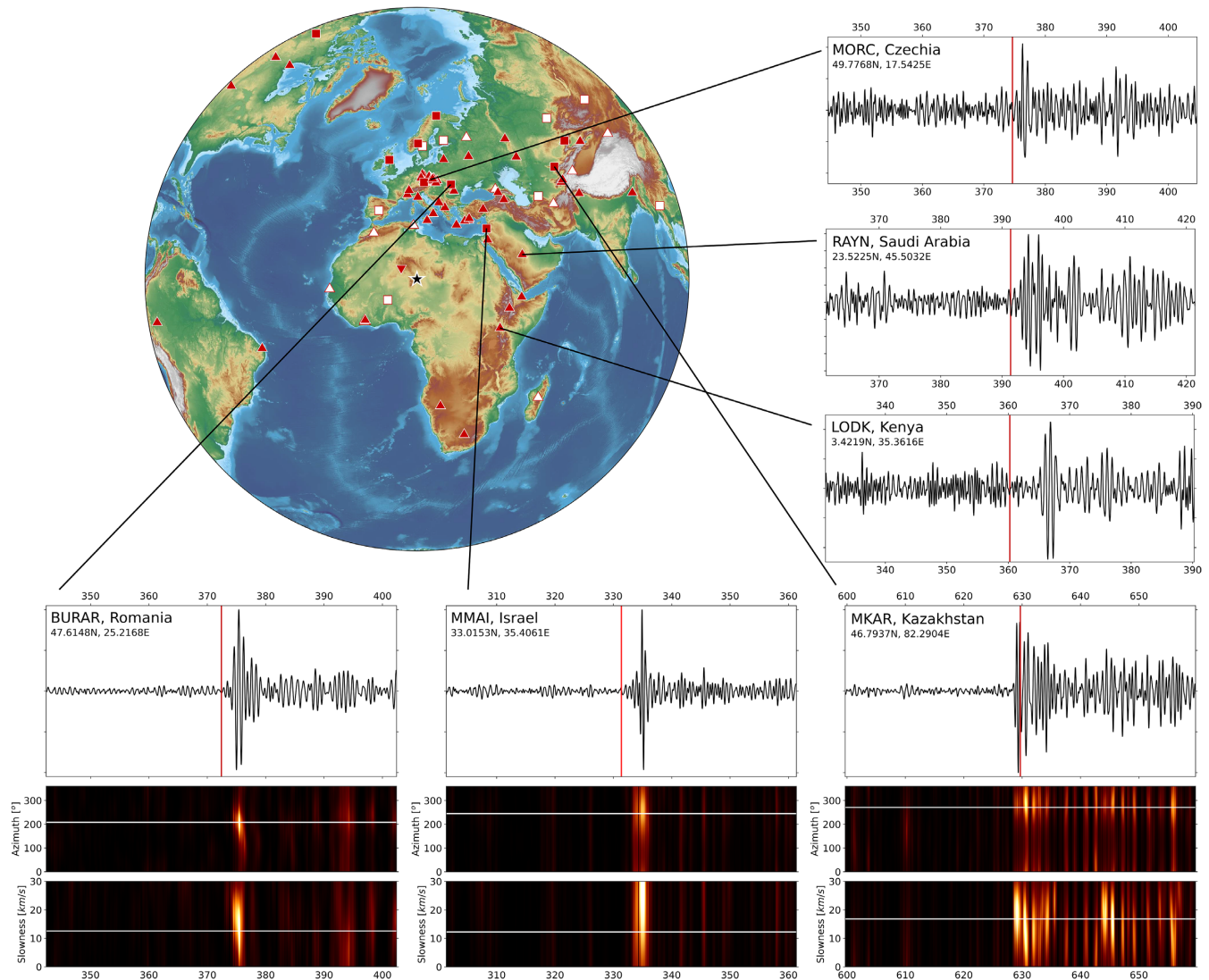


**Figure 2.** Global station distribution (symbols as in Fig. 1). Left-hand panels show three vertical component velocity waveforms, filtered between 1–3 Hz, from three-component instruments RAYN, MORC and LODK. Vertical red line shows the predicted  $P$ -wave arrival, based on the NEIC location. Lower panels show data from three small-aperture seismic arrays (Bucovina, Mount Meron, and Makanchi), again filtered between 1–3 Hz. Top panel shows the beamformed waveform, based on the NEIC location. Lower panels show sweeps through slowness and azimuth space (cf. Davies *et al.* 1971), with colour indicating array coherence using the  $F$ -statistic (e.g. Blandford 1974). White lines show the predicted slowness and azimuth for  $P$ -wave arrivals from the Ténéré earthquake.

of identifying a confirmed signal above the level of noise. We see no unmistakable depth phases, which would offer a high-precision constraint on the event depth. A few stations show multiple bursts of energy but there is insufficient evidence at any station to label with confidence the later arrivals as depth phases.

Summarizing the available seismological data, we are left with a comparatively sparse set of phase observations, of variable, but

often limited, precision. The advantages in signal identification and arrival precision that arise from the enhanced processing of small aperture arrays are clear. But only a few of the operators of these stations make their waveform data Open Access (see Fig. 2). Similarly, many of the more isolated three-component stations, vital for filling gaps in azimuthal and epicentral coverage, remain closed to the general public. Combined, these pose the question of how

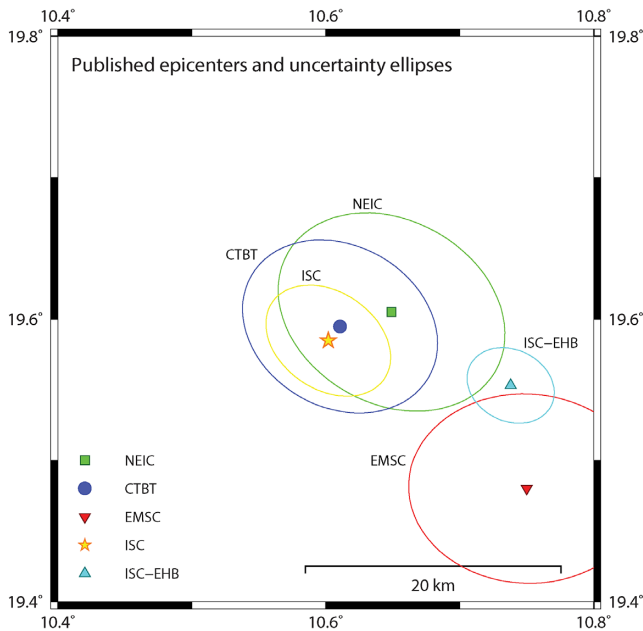


**Figure 3.** Published location estimates and corresponding 95 per cent confidence ellipses for the 2017 January 18, Niger Earthquake. The epicentres are as provided in Table 1 and the 95 per cent confidence ellipses have (Smaj/Smin/Azimuth) parameters (18.7/14.4/125°) NEIC, (16.0/12.7/120°) CTBT, (18.5/14.9/93°) EMSC, (10.6/7.6/125°) ISC and (7.1/5.6/117°) ISC-EHB with Smaj and Smin given in km.

reliable high-precision earthquake location is on closed-access data, and how well characterized events such as the Ténéré earthquake can be, using only Open Access seismic data.

### 3 SEISMIC LOCATION ESTIMATES FOR THE 2017 JANUARY 18 NIGER EARTHQUAKE

Fig. 3 shows the epicentres listed in Table 1 together with their published 95 per cent confidence ellipses. The epicentres reported by the NEIC/USGS (National Earthquake Information Center/United States Geological Survey) and CTBTO/IDC (Comprehensive Nuclear Test-Ban-Treaty Organization/International Data Center) lie comfortably within the confidence ellipse reported by the other agency, and there is significant overlap between the two confidence ellipses. The epicentre reported by the International Seismological Center (ISC 2021) lies within both of these confidence ellipses but is itself associated with a much smaller confidence ellipse which does include the CTBT epicentre estimate, but not the NEIC epicentre estimate. A fourth location estimate is provided in the ISC catalogue summary: the ISC-EHB estimate (ISC-EHB 2021), named after Engdahl, van der Hilst and Buland. This epicentre lies to the southeast and outside of all of the other 95 per cent confidence ellipses. The ISC-EHB estimate itself is associated with a far smaller confidence ellipse which overlaps little with the other 95 per cent confidence ellipses. All of these confidence ellipses share a similar azimuth of the semi-major axis: all around 120°. This is easy to understand in terms of the station distribution (cf. Fig. 2) since the density of contributing stations in directions from North to East (i.e. in Europe and Central Asia) is substantially greater than in other directions. The final location estimate is that from the European Mediterranean Seismological Center (EMSC, e.g. Godey *et al.* 2013) and this lies

approximately 20 km to the South East of the ISC and CTBT locations. Like the NEIC estimate, the EMSC solution is published fairly rapidly and is attributed a relatively large confidence ellipse. However, the EMSC solution is more dominated by stations to the North (Europe) than the NEIC solution which is consistent with the rather different epicentre estimate and orientation of the confidence ellipse. Given the discrepancy between the EMSC solution and the ISC and CTBT locations, we will not be subjecting the EMSC solution to further analysis.

Comparing the various epicentres and corresponding confidence ellipses is difficult since the solutions use varying combinations of arrival-time readings, station distributions, weights and location algorithms. Only the NEIC, CTBT and EMSC catalogues are truly independent. Although the solutions have a number of stations in common, the readings are made by different analysts and using different systems and location procedures. The ISC catalogue, and the ISC-EHB solution, exploit phase readings from multiple catalogues and can frequently use two or more alternative arrival time estimates, reported by different agencies, for the same phase arrival to constrain an event. TORD in southwestern Niger and KEST in Tunisia are two of the stations in the ISC bulletin that are closest to the earthquake epicentre (see Fig. 1). Both stations are primary seismic stations of the IMS and, to the best of our knowledge, the data from neither are available to users other than those with access authorized by National Data Centers in the CTBT system. The USGS has access to this data via the United States National Data Center and is authorized to use arrival-time estimates from these stations when forming their earthquake bulletin.

The ISC bulletin provides two estimates for the  $P_n$  arrival time at TORD: 21:50:53.534 and 21:51:02.71, reported by the IDC and the NEIC respectively. Only the first of these is a defining phase in the ISC catalogue, with a time residual of  $-0.7$  s. The second is labelled a ‘Questionable onset’ (with a time residual of 8.5 s) and does not contribute to the solution. The ISC bulletin also provides two estimates for the  $P_n$  arrival time at KEST: 21:52:07.30 and 21:52:06.98, again provided by the IDC and the NEIC, respectively. Both of these arrivals (with time residuals of  $-0.7$  and  $-1.0$  s, respectively) are defining arrivals in the ISC solution. In the ISC-EHB bulletin, all four of these arrival times are defining phases for the location estimates with time residuals listed as  $-2.1$  s (TORD  $P_n$ , IDC), 7.1 s (TORD  $P_n$ , NEIC),  $-1.4$  s (KEST  $P_n$ , IDC) and  $-1.7$  s (KEST  $P_n$ , NEIC). The time residual on the TORD  $P_n$  arrival is large for both the ISC and ISC-EHB solutions. The size of the time residual led it to be disregarded from the ISC solution. While it is a defining phase in the ISC-EHB solution, it is not easy to estimate the effect it has on the solution without a thorough examination of the weights and the provenance of the location algorithm.

The discrepancy between the ISC-EHB epicentre and the other epicentres is likely a combination of many such differences. The waveforms displayed in Figs 1 and 2 make it clear how emergent and ambiguous some of the phase arrival time estimates may be. Often the highest amplitude comes several seconds after what appears to be the first signal onset and we may have to make judgements regarding what is a likely first  $P$ -arrival and what is a possible depth phase. The first part of the signal visible above the background noise may be significantly later than the true onset time if we have an emergent signal or a depth phase with a higher amplitude than the first  $P$ -arrival. Without access to the waveform data, it is not possible for an independent seismologist to evaluate the quality of the arrival time estimates, limiting our ability to determine where pick uncertainty may be driving the discrepancies in location estimates. The

seismic event location procedures employed at the different agencies are under continual revision and overviews of recent progress at the NEIC and IDC are given by Benz (2017) and Koch (2013) respectively. Details of improvements to the ISC location algorithm can be found in Bondár & Storchak (2011), and references therein. A comprehensive description of the exact procedures employed at a given observatory, so detailed that they could be reproduced exactly by a different observatory, is unrealistic.

However, we can gain more understanding as to how the location estimates depend upon the choice of stations alone by performing new location estimates using a common algorithm with the arrival times used for the different catalogues displayed in Fig. 3. We use the Bayesloc program (Myers *et al.* 2007) which can solve for the locations of multiple seismic events simultaneously by a Monte Carlo Markov Chain (MCMC) procedure to find a joint probability distribution for the events' origins, origin parameter uncertainties, and for empirical corrections to modelled traveltimes. Prior constraints, for example Ground Truth event locations or existing models for traveltime corrections, can be applied if available to improve the quality of the posterior probability distributions. Although the program is designed for, and is most effective with, large clusters of seismicity, it can also be run for a single event. Having only a single event of course precludes, for example, the calculation of empirical traveltime corrections (since we cannot resolve between the contributions to arrival-time anomalies resulting from velocity variations and those resulting from picking errors). For each iteration of the MCMC routine, the program writes out the epicentre coordinates. Over a single run, many thousands of origin hypotheses are written out generating a cloud. The size and shape of this cloud provides a visualization of the uncertainty associated with the location which may show a more complex geometry than the classical formal confidence ellipses. Given the absence of prior constraints, and the fact that we only have a single event, our main motivation for using Bayesloc is this ability to visualize any irregularities in the geometry of the location probability distribution.

Fig. 4 displays the clouds of trial epicentre estimates from the Bayesloc calculations for four different combinations of stations. In panel (a), the event is located using only the phase arrival times listed in the USGS/NEIC bulletin. The red symbols are the epicentres output when we only use those stations for which waveform data can be obtained without barrier by an arbitrary user from only open sources (red symbols in panel b). The grey symbols are the epicentres output when we also allow use of the arrival times from stations for which waveform data are not available without specific authorization (white symbols in panel b). We attempt to better visualize the spread of the point clouds by plotting the 90, 95 and 99 per cent confidence ellipses based upon the statistics of the coordinates, although we stress that the point cloud distributions may display significant departures from the geometries indicated by the ellipses. The inclusion of the closed access stations reduces the apparent spread somewhat although the difference is not large. As noted earlier, the TORD arrival in this data set is associated with a large time residual and so it may have had very little influence on the solutions. We note also that the Bayesloc epicentre clouds using the USGS/NEIC arrival estimates are consistent with the bulletin epicentre estimate.

Panel (c) of Fig. 4 shows the corresponding Bayesloc epicentre clouds for the arrivals listed in the ISC bulletin, with the corresponding station maps displayed in panel (d). There is a significant difference between the spread of the epicentre clouds for the 'complete' and 'strictly open' station networks for the ISC arrivals. We note that not only is the TORD time residual far smaller for one

of the arrivals in the ISC solution, but there are 3 other network stations, KIC, TIC and LIC which add extra constraints from the South West. These stations are all very close to DBIC, in the Ivory Coast, and they do not much increase the azimuthal coverage. However, their inclusion may change the weight of the constraints from that direction considerably. We note in addition, an extra constraint from the Sonaca Array (ESDC) in Spain from the CTBT bulletin. This is in a direction in which there are no open stations with good signals or clear picks. This may be an example of where the use of beamforming of signals on a seismic array may make a usable phase arrival where one was not sufficiently strong on a single channel, allowing the identification of arrivals even in regions where the radiation pattern leads to comparatively low amplitudes. The Bayesloc epicentre clouds lie a few kilometres to the South East of the ISC bulletin epicentre, and to the West of the epicentre provided in the ISC-EHB bulletin. The differences in the location estimates are likely due to both different weightings of the phase arrivals and differences in the location algorithms.

To summarize, with the available seismic stations, there is a lateral uncertainty of at least 10 km in the epicentral estimates. The epicentre from the ISC-EHB bulletin appears to be an outlier and, given the set of arrivals from which this solution is formed, the quoted 95 per cent confidence interval would appear to be optimistic. We can move the epicentre estimate by several kilometres by changing the observing network alone, but never by more than around 10 km. Had the seismic signals from this event had characteristics of an explosion, the confidence region from the seismic signals is sufficient for the criteria for a permissible On-Site-Inspection following Entry Into Force of the Comprehensive Nuclear Test-Ban-Treaty. The treaty text states 'The area of an on-site inspection shall be continuous and its size shall not exceed 1000 square kilometres. There shall be no linear distance greater than 50 kilometres in any direction' (UN 1998). Even with the existing network (and there are no non-IMS stations in the bulletins considered here at any significantly closer distances or covering any significant azimuthal gaps), Fig. 4 indicates that the location uncertainty is well within these limits. The completed IMS, as listed in the treaty text, contains in addition stations not currently operating that would likely have improved the constraints on this event (in particular, the Luxor array in Egypt: 26.0°N 33.0°E, not yet constructed, and the BGCA three-component station in the Central African Republic: 5.176°N, 18.424°E, installed but not currently operational). Another IMS three-component station, KOWA, in Mali, is now operational but was not at the time of this earthquake (data from IU.KOWA is openly available to the community via IRIS). There are few opportunities for further reducing the uncertainty in the seismic location estimates without additional, closer, stations. For example, there are no nearby seismic events from which we could perform a calibrated or relative location estimate (e.g. Douglas 1967, and subsequent studies of joint epicentral determination and multiple event location). The scarcity of seismic observations in the region also means that regional 3-D seismic velocity models remain unrefined and uncalibrated.

#### 4 SURFACE DISPLACEMENT FROM THE 2017 JANUARY 18 NIGER EARTHQUAKE USING INSAR DATA

In the case of remote continental earthquakes, with a sparsity of near-field seismological data, the recently developed global coverage of satellite radar offers an additional data set to which may help

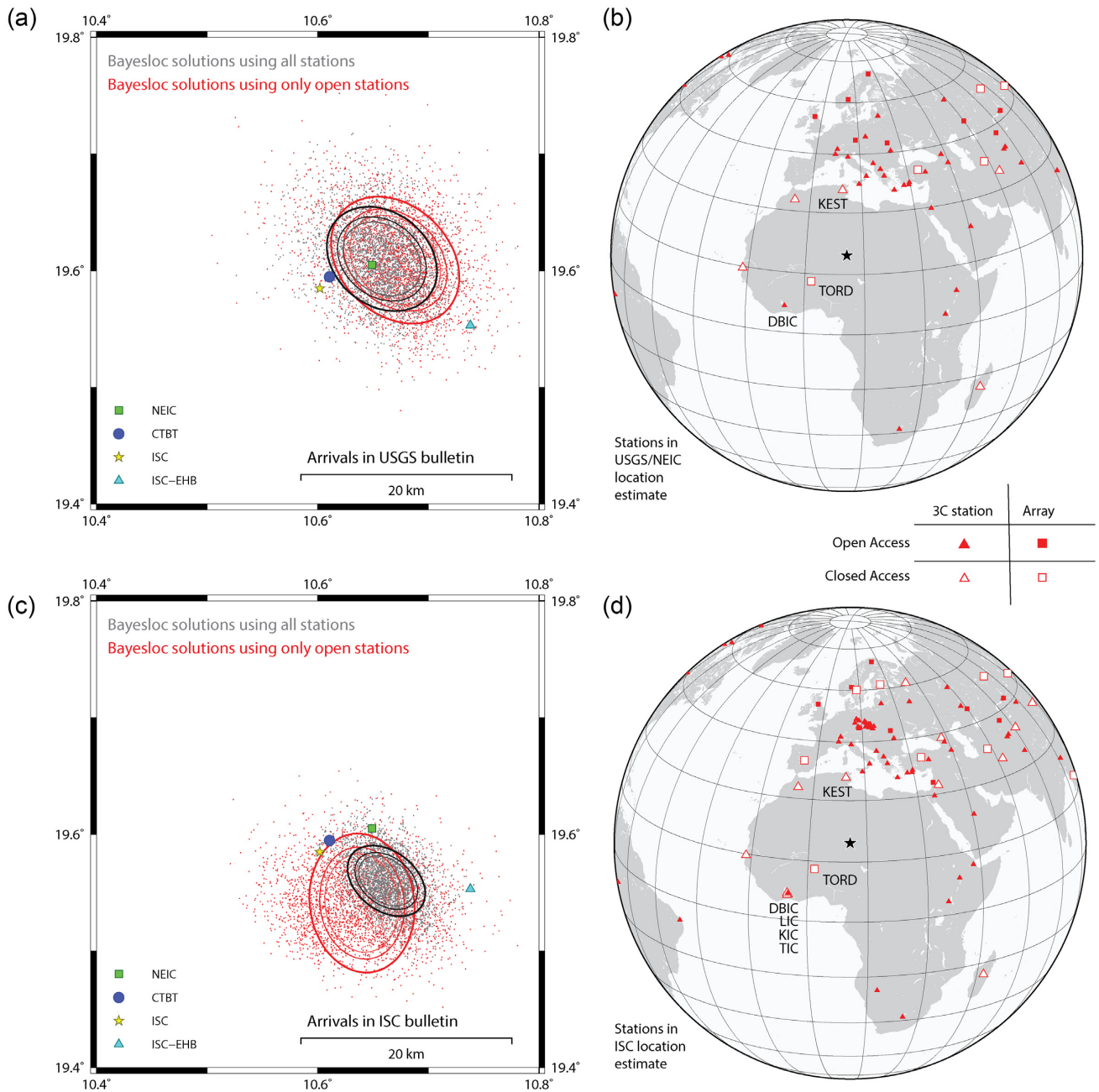


**Figure 4.** Location estimates obtained using the Bayesloc program with station selections as indicated. Panels (a) and (c) display clouds of the epicentres in the Bayesloc MCMC together with the 90, 95 and 99 per cent confidence ellipses calculated for the scatter plots. Each cloud contains 36 000 points. Panels (b) and (d) display the stations used to obtain the solutions displayed in panels (a) and (c), respectively. Key stations are labelled. Stations DBIC, KIC, TIC and LIC are within tens of kilometres of each other such that they almost appear co-located when displayed on a global scale.

constrain earthquake locations, and complement those constraints available from seismology. The limiting factor in locating an earthquake using satellite geodesy is not directly the magnitude of the earthquake, but instead the amplitude of the surface deformation, and whether any signal can be detected. Whilst the Ténéré earthquake is lower magnitude than typically studied using InSAR (e.g. Weston *et al.* 2012; Funning & Garcia 2019), other small-magnitude events have been detected in the past (Lohman & Simons 2005; Ritz *et al.* 2020), in cases where the earthquake is very shallow, allowing higher amplitude near-fault displacements to be expressed at the surface. Whereas converting remote seismological observations to an source location can be subject to major uncertainties on the

scale of tens of kilometres, particularly relating the velocity structure, geodetic measurements offer the direct detection of near-fault displacement, in the ideal case where a fault breaks the surface, can determine the fault location with pixel-scale resolution (typically tens of metres). Therefore, whilst InSAR offers no constraint on the earthquake origin time, places no constraints on the rupture evolution, and, for small-magnitude events, can only detect shallow sources (Mellors *et al.* 2004), it can offer a valuable complement to seismological observations, placing precise constraints on the location of the rupture plane.

To supplement the available seismic data, we process InSAR images for the source region using data from the European Space

Agency's Sentinel-1 satellites. We use acquisitions that span the earthquake date, and construct interferograms using all potential pairs where the earthquake occurs within a time span of up to four consecutive acquisitions (Fig. 5). Processing was carried out using the LiCSAR system (Lazecký *et al.* 2020, to which readers are directed for a full description of the processing approach). Each interferogram is processed using multilooking factors of 5 in range and 20 in azimuth, with interferograms therefore having a spatial resolution of  $\sim 100 \times 100$  m per pixel. Data are then subject to spatial filtering using an adaptive power spectrum filter. Due to the remote location, only ascending track data were being routinely acquired at the time of our study earthquake, with a 12-d repeat time. Coherence in the region at such short temporal baselines is good—the region is unvegetated desert, and whilst migratory sand can cause problems for radar interferometry, this does not appear to be the case around our earthquake, although we note that the dune fields to the south and southwest show markedly lower coherence. In Supporting Information, Fig. S2 shows average coherence prior to spatial filtering at 12, 24 and 36 d temporal baselines across the whole Sentinel-1 archive. As demonstrated by Figs 5 and 6, after spatial filtering, coherence at the wavelengths of interest for earthquake-related processes is extremely high. Given the lack of major topographic features, there is minimal topographically correlated atmospheric noise, although all interferograms are subject to long-wavelength noise presumed to result from a combination of atmospheric variations and orbital effects (see Figs 5 and 6). One SAR acquisition (20161216) features NE-SW orientated bands which are clearly unrelated to either the regional tectonics or our study earthquake. Although the exact origin of these features is uncertain, they are most likely to be atmospheric rolls. Some of the interferograms shown in Fig. 6, which do not span the earthquake, show significantly higher levels of noise, which we presume to be atmospheric in origin, showing that even here, atmospheric variability can strongly influence the detection of tectonic signals, although it does not hinder our observations of the 2017 Ténéré earthquake.

All coseismic interferograms feature a small, roughly circular, displacement signal at  $\sim 19.6^\circ$  N,  $10.6^\circ$  E, highlighted by the black circle on Fig. 5. This signal displays a spatial pattern as expected for a small-magnitude earthquake, is at a wavelength where we would expect the deformation signal from an  $m_b$  4.3 to be (1–5 km, based on a rupture length of  $\leq 1$  km following the established earthquake scaling relationships; Wells & Coppersmith 1994), is common to all interferograms that span the earthquake date, and is not present in any interferograms that do not span the earthquake (see Fig. 6, for examples). We are therefore confident that this signal relates to our study earthquake, despite the small amplitude of the observed signal.

To improve the resolution of this signal, we construct a simple linear stack of three fully independent interferograms (20161204–20170202, 20161228–20170226 and 20170109–20170310 from Fig. 5—stack shown in Fig. 7a). To remove long-wavelength atmospheric effects, and to isolate signals at wavelengths likely to be related to an  $m_b$  4.3 earthquake, we spatially filter the InSAR data using a four-pole Butterworth filter, bandpassed between 15000 and 500 m (Fig. 7b).

The resulting stack shows a clear, coherent line-of-sight displacement of up to 6 mm. Only one lobe of the deformation field is clearly visible, and although there are indications on the filtered stack of opposite-polarity displacement lobes to the northeast and southeast of the main deformation lobe, these are insufficiently clear to permit the determination of a focal mechanism. We visually assess that the causative fault plane most likely lies to the southeast or northeast

of the peak in displacement. The lack of a clear four-lobe pattern of deformation argues against a pure strike-slip mechanism, and we infer that the earthquake therefore involved either dip- or oblique-slip faulting.

The deformation pattern shows no clear discontinuities in phase, either on the stack or on individual interferograms, suggesting that the rupture did not break the surface, and that the top of the fault rupture patch is buried. That there is an observable signal at all, however, from such a small-magnitude event, indicates that the earthquake must have been shallow ( $\leq 5$  km; see Mellors *et al.* 2004, Dawson & Tregoning 2007), consistent with the lack of any clearly separated depth phases in the seismic data (see Fig. 2). In the case of this earthquake, located in the sandy Ténéré desert, we consider it likely that the earthquake ruptured to the top of the consolidated bedrock, but that the deformation signal is subsequently blanketed by overlying less consolidated sandstones, less able to sustain coseismic rupture.

## 5 CONCLUSIONS AND DISCUSSION

Fig. 7 shows both seismological and geodetic constraints on the location of the 2017 Ténéré earthquake. Of the four catalogue locations published by seismological agencies only those from the CTBT and the initial ISC catalogue are consistent with the more precise location information offered by the InSAR displacement pattern. The location from the NEIC lies marginally too far east, but within its own uncertainty envelope of the geodetic location, whilst the ISC-EHB location lies  $\sim 15$  km to the east-southeast of the geodetic location, substantially beyond its quoted uncertainty interval from the geodetically observed displacement signal (Fig. 3). The EMSC location lies  $\sim 30$  km to the southeast of the detected surface deformation—the furthest of any of the catalogue locations we consider.

Such differences between seismological and geodetic locations are commonly, and widely observed for larger earthquakes (e.g. Weston *et al.* 2012). However, comparison of geodetic and seismological location is not simple—the two approaches are measuring slightly different aspects of the earthquake. Seismological locations like those applied to this earthquake give a hypocentre—the point of rupture initiation. In contrast, geodetic data like that used here has no capacity to constrain the earthquake initiation, or its rupture process, in time, as the displacement seen in the interferograms is the result of the complete earthquake rupture. In this case, we are unable to solve robustly for a causative fault plane from the InSAR data, but even if we could, the earthquake hypocentre could still lie anywhere on that rupture plane. For larger earthquakes, with rupture lengths of  $> 5$  km, this can pose additional location problems. However, for a small-magnitude event like the 2017 Ténéré earthquake, where the rupture length is likely to be  $< 5$  km, this discrepancy between the seismological hypocentre and the geodetic fault rupture will be small, compared to the uncertainties in seismological location.

Seismological locations are subject to uncertainty in the solid-Earth velocity structure along the full ray path from source to receiver. In the case of the locations shown in Figs 3 and 4, the relative traveltimes difference between all the locations shown is  $< 0.5$  s for regional arrivals and  $< 0.2$  s for teleseismic arrivals. As demonstrated in Fig. 2, the majority of arrivals are emergent, and picking a precise onset is usually subject to uncertainties on at least this magnitude. This is then compounded by the variation in predicted

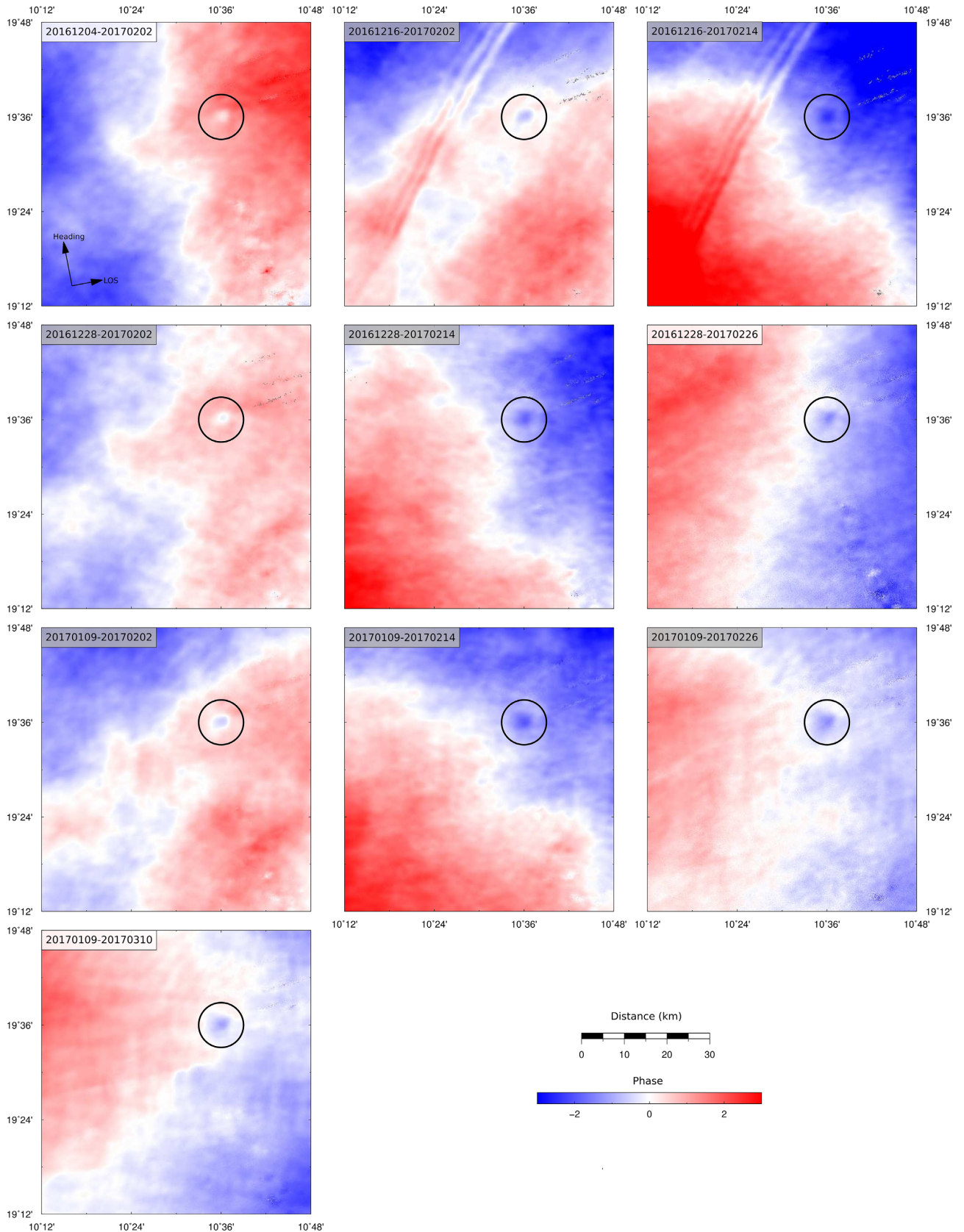


**Figure 5.** 10 coseismic interferograms, unwrapped. We show equivalent wrapped interferograms in Fig. S1 in the Supporting Information. Colour scale shows multiples of the complete phase cycle. Numeric codes in the top left of each panel indicate the SAR acquisitions used to produce each interferogram. Shading behind numeric codes indicates those independent pairs used in the stack shown in Fig. 7. Black circle highlights the consistent signal identified as results from the earthquake. The final panel shows the InSAR coherence for a single interferogram.

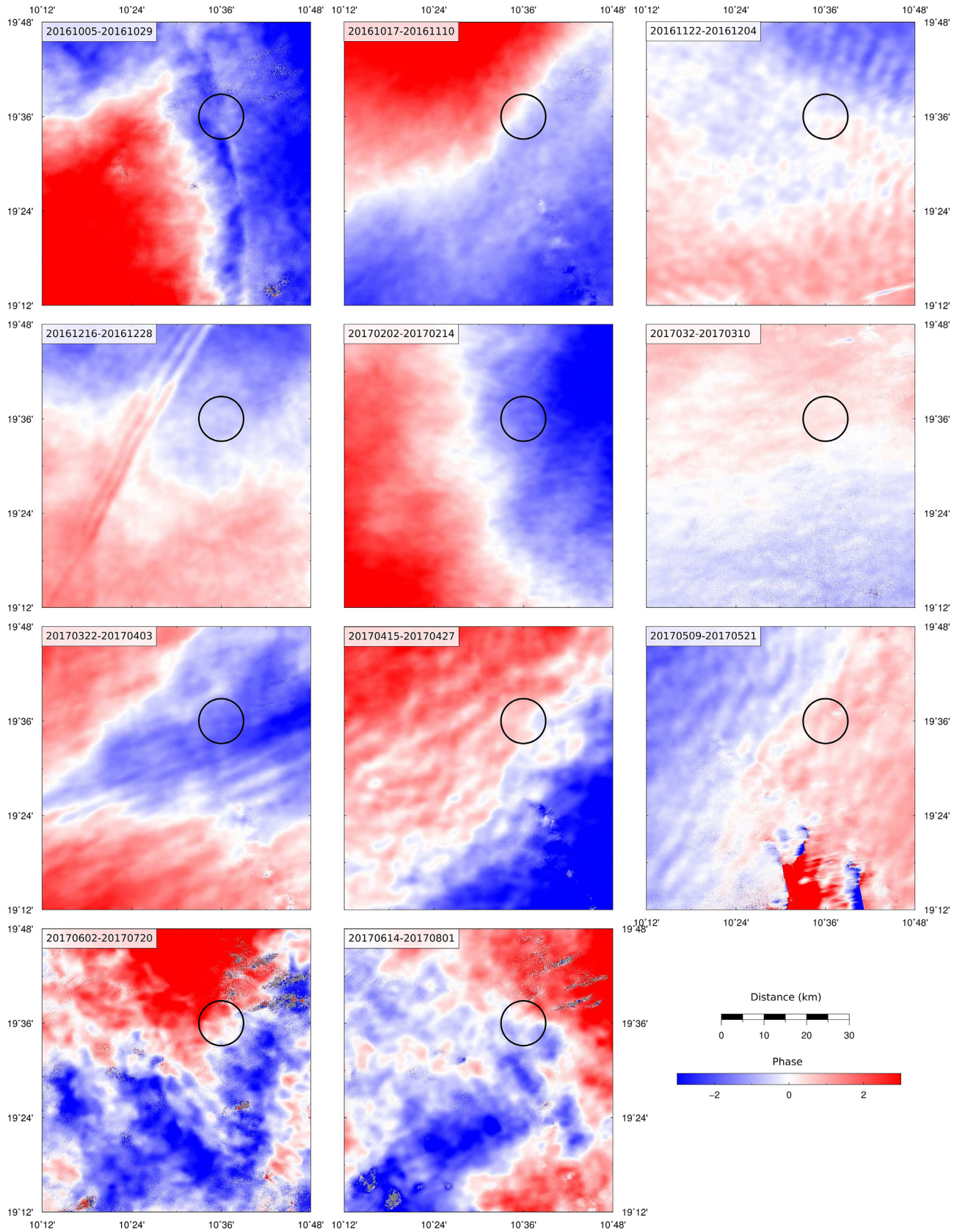


**Figure 6.** 11 interferograms, unwrapped, that do not span the date of the Ténéré earthquake. Numeric codes in the top left of each panel indicate the SAR acquisitions used to produce each interferogram. Black circle highlights area in which the coseismic interferograms shown in Fig. 5 show a consistent deformation signal.

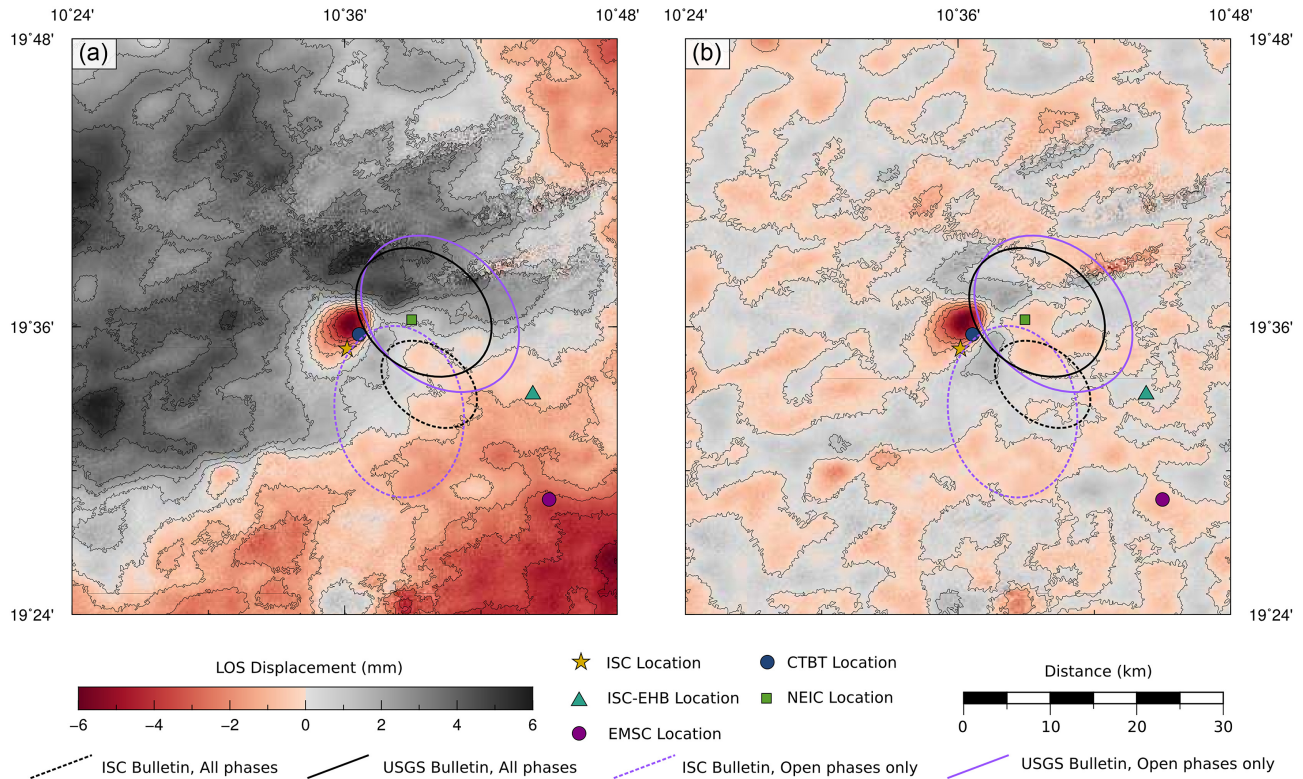


**Figure 7.** (a) Stacked unwrapped interferogram. (b) Stacked interferogram, filtered between 15 km and 500 m. Colour scale shows line-of-sight displacement. Symbols show seismological locations, as in Fig. 3. Contours show 95 per cent interval ellipses determined using different seismic arrival subsets, as described in Fig. 4.

traveltimes between different velocity models. Many location routines use a standard global 1-D velocity structure. Inclusion of the 3-D Earth structure, whilst possible (e.g. Simmons *et al.* 2021, and references therein), remains subject to relatively large uncertainties in areas like Saharan Africa, where coverage from both sources and stations is very poor. In this region, the variation in predicted traveltimes between simple 1-D and more complex 3-D velocity models can add an additional 0.5 s in traveltime uncertainty, equating to a spatial difference on the order of 10–20 km. In contrast, locations based on geodetic data are subject to uncertainty derived only from the very-near source elastic structure. For shallow earthquakes, in particular, the impact that this has on geodetic earthquake location is minimal.

Seismological estimates for the magnitude of the Ténéré earthquake vary between  $m_b$  4.2 (IDC) and  $m_b$  4.7 (EMSC). Although without formally determining the amount of slip, we are unable to use the InSAR data to quantitatively estimate a comparable geodetic magnitude, we note that that surface displacement wavelength of the deformation imaged using InSAR is perhaps longer than would be expected, particularly at the lower end of the range of  $m_b$  estimates. As the InSAR deformation field captures all deformation between the two acquisition dates, we cannot rule out the possibility that the displacement seen is enhanced by some level of aseismic process. However, this would be rare for an earthquake of this magnitude.

The consideration of both InSAR and seismological data for small magnitude earthquakes, as shown here, therefore demonstrates the potential for geodetic data to both supplement, and potentially calibrate, seismological earthquake location, allowed the determination of high-precision absolute spatial locations for small earthquakes

with small rupture lengths. Such characterization has several potential applications. First, such high precision location constraints have the potential to contribute to the monitoring and discrimination capabilities of the CTBT, particularly in remote areas, far from near-field seismological instrumentation. Secondly, high-precision geodetic earthquake locations can be used to calibrate regional seismological locations, which are often subject to large systematic uncertainties due to biases in velocity structure and in network geometry. Thirdly, in cases where accurate arrival times can be determined, precise locations allow the use of small earthquakes in remote places to be used for the validation of tomographic models for the solid-Earth velocity structure, supplementing sparse available equivalents from controlled-source seismic signals (usually explosions: Bondár & McLaughlin 2009).

Our study on the 2017 Ténéré earthquake therefore illustrates the potential for satellite radar to supplement the monitoring capabilities of traditional seismological networks for earthquake location, particularly in remote areas, and particularly in areas with high coherence. As the footprint of satellite missions, and the coverage of routine processing, expands, the potential for InSAR to be brought in to routine earthquake monitoring will only increase. Seismic detectability maps have long been employed to estimate thresholds for the magnitudes of seismic disturbances which can confidently be detected and location in a given region for a given monitoring network (e.g. Kväerna & Ringdal 2013). Going forwards, we would recommend developing from the theoretical work of Mellors *et al.* (2004) and Dawson & Tregoning (2007), and building towards global detectability maps for geodetic observation, although we recognize that these would need to be built in the limitations posed by the trade-off between depth and magnitude of displacement detectability, and

time-variable nature of both decorrelation and non-tectonic (e.g. atmospheric) noise in satellite radar. Funning & Garcia (2019) suggested that there is a magnitude completeness threshold for global earthquake detectability for crustal earthquakes between  $M_w$  6.2–7.0 when using Sentinel-1 InSAR data. However, our study, along with a growing number of others (e.g. Ganas *et al.* 2017; Dalaison *et al.* 2021; Liu *et al.* 2021), shows that, whilst far from complete, in certain regions and for particularly shallow earthquakes, there are often detectable signals even for earthquakes down to an  $M \sim 4$  which can be used to provide additional constraints on earthquake locations.

The 2017 Ténéré earthquake also illustrates the role that data not routinely available to the academic community play in earthquake location. For both the USGS and the ISC sets of arrivals used in our relocation (see Fig. 4), restricting the arrivals used to only Open Access data leads to a marked increase the location uncertainty. Whilst the InSAR data used here, from the European Space Agency's Sentinel-1 mission, is freely available, the same is not necessarily true for all radar missions. Whilst the radar coherence in the Ténéré is high, allowing up to resolve such small displacements, conducting such work elsewhere, particularly in more vegetated environments, will likely benefit from the use of a range of satellites with different mission parameters, particularly wavelength, and may lead to a similar disparity between Open Access and restricted data that we see in the seismological data sets.

## ACKNOWLEDGMENTS

TJC was supported in this work by the Royal Society under URF\R1\180088. TJC was also supported through COMET, the UK Natural Environment Research Council's Centre for the Observation and Modelling of Earthquakes, Volcanoes, and Tectonics. We thank Milan Lazecky for his assistance with processing the InSAR data, and Tim Wright for useful discussions. We thank Manon Dalaison and one anonymous reviewer for their comments, which have helped improve this manuscript.

All maps in this paper are created using GMT software (Wessel *et al.* 2019). Seismograms in Figs 1 and 2 were plotted using Obspy (Beyreuther *et al.* 2010).

## DATA AVAILABILITY

The published location estimates were obtained from the bulletin of the ISC (2021) [http://www.isc.ac.uk/cgi-bin/web-db-v4?event\\_id=619603285](http://www.isc.ac.uk/cgi-bin/web-db-v4?event_id=619603285) (last accessed 2022 February) and from the EMSC <https://www.emsc-csem.org/Earthquake/earthquake.php?id=561096> (last accessed 2022 February). The USGS/NEIC solution with phase arrival times are published on <https://earthquake.usgs.gov/earthquakes/eventpage/us10007u0v/executive> (United States Geological Survey, last accessed 2022 February). The bayesloc program is obtained from <https://www-gs.llnl.gov/nuclear-threat-redaction/nuclear-explosion-monitoring/bayesloc> (last accessed 2022 February). InSAR data we retrieved from <https://comet.nerc.ac.uk/comet-lics-portal/> (last accessed February 2022). LiCSAR data contain modified Copernicus Sentinel data [2017] analysed by the Centre for the Observation and Modelling of Earthquakes, Volcanoes and Tectonics (COMET). LiCSAR uses JASMIN, the UK's collaborative data analysis environment (<http://jasmin.ac.uk>)

Seismic waveform data were obtained from the following networks of the International Federation of Digital Seismograph Networks (FDSN): BR, CA (doi:10.7914/SN/CA),

CN (doi:10.7914/SN/CN), CQ (doi:10.7914/SN/CQ), G (doi:10.18715/GEOSCOPE.G), GE (doi:10.14470/TR560404), GO, GR (doi:10.25928/mbx6-hr74), GT (doi:10.7914/SN/GT), HL (doi:10.7914/SN/HL), HP (doi:10.7914/SN/HP), HT (doi:10.7914/SN/HT), II (doi:10.7914/SN/II), IS, IU (doi:10.7914/SN/IU), KO (doi:10.7914/SN/KO), KR (doi:10.7914/SN/KR), KZ (doi:10.7914/SN/KZ), MN (doi:10.13127/SD/FBBBTDTD6Q), NR (doi:10.7914/SN/NR), RO (doi:10.7914/SN/RO), TJ (doi:10.7914/SN/TJ), US (doi:10.7914/SN/US) and XW (doi:10.7914/SN/XW\_2017). We gratefully acknowledge the operators of all of the networks for providing open access to the data and to the Incorporated Research Institutions for Seismology (IRIS, <https://www.iris.edu/hq/>) and the various nodes of the European Integrated Data Archive (EIDA, <https://www.orfeus-eu.org/data/eida/nodes/>) for providing access to this data.

## REFERENCES

- Barker, B. *et al.*, 1998. Monitoring nuclear tests, *Science*, **281**(5385), 1967–1968.
- Benz, H., 2017. Building a National Seismic Monitoring Center: NEIC from 2000 to the Present, *Seismol. Res. Lett.*, **88**(2B), 457–461.
- Beyreuther, M., Barsch, R., Krischer, L., Megies, T., Behr, Y. & Wassermann, J., 2010. ObsPy: a Python toolbox for seismology, *Seismol. Res. Lett.*, **81**, 530–533.
- Blandford, R., 1974. An automatic event detector at the Tonto Forest Seismic Observatory, *Geophysics*, **39**(5), 633–643.
- Bondár, I. & McLaughlin, K., 2009. A new ground truth data set for seismic studies, *Seismol. Res. Lett.*, **80**, doi:10.1785/gssrl.80.3.465.
- Bondár, I. & Storchak, D., 2011. Improved location procedures at the International Seismological Centre, *Geophys. J. Int.*, **186**(3), 1220–1244.
- Bondár, I., Myers, S.C., Engdahl, E.R. & Bergman, E.A., 2004. Epicentre accuracy based on seismic network criteria, *Geophys. J. Int.*, **156**(3), 483–496.
- Chun, K.Y., Wu, Y. & Henderson, G.A., 2011. Magnitude estimation and source discrimination: a close look at the 2006 and 2009 North Korean underground nuclear explosions, *Bull. seism. Soc. Am.*, **101**(3), 1315–1329.
- Dalaison, M., Jolivet, R., van Rijsingen, E. & Michel, S., 2021. The interplay between seismic and aseismic slip along the Chaman Fault illuminate by InSAR, *J. geophys. Res.*, **126**, doi:10.1029/2021JB021935.
- Davies, D., Kelly, D.J. & Filson, J.R., 1971. The VESPA process for the analysis of seismic signals, *Nature*, **232**, 8–13.
- Dawson, J. & Tregoning, P., 2007. Uncertainty analysis of earthquake source parameters determined from InSAR: a simulation study, *J. geophys. Res.*, **112**, doi:10.1029/2007JB005209.
- Douglas, A., 1967. Joint epicentre determination, *Nature*, **215**(5096), 47–48.
- Funning, G. & Garcia, A., 2019. A systematic study of earthquake detectability using Sentinel-1 Interferometric Wide-Swath data, *Geophys. J. Int.*, **216**, doi:10.1093/gji/ggy426.
- Ganas, A., Kourkoulis, P., Briole, P., Moshou, A., Elias, P. & Parcharidis, I., 2017. Coseismic Displacements from Moderate-Size Earthquakes Mapped by Sentinel-1 differential interferometry: the case of February 2017 Gulpinar Earthquake Sequence (Biga Peninsula, Turkey), *Remote Sens.*, **10**, doi:10.3390/rs10071089.
- Gibbons, S.J., Antonovskaya, G., Asming, V., Konechnaya, Y.V., Kremetskaya, E., Kværna, T., Schweitzer, J. & Vaganova, N.V., 2016. The 11 October 2010 Novaya Zemlya Earthquake: implications for velocity models and regional event location, *Bull. seism. Soc. Am.*, **106**(4), 1470–1481.
- Godey, S., Bossu, R. & Guilbert, J., 2013. Improving the Mediterranean seismicity picture thanks to international collaborations, *Phys. Chem. Earth, Parts A/B/C*, **63**, 3–11.
- ISC, 2021. *International Seismological Centre on-line Bulletin*, doi:10.31905/D808B830.

- ISC-EHB, 2021. *International Seismological Centre ISC-EHB dataset*, doi:10.31905/PY08W6S3.
- ISC-GEM, 2021. *International Seismological Centre ISC GEM earthquake catalog*, doi:10.31905/d808b825.
- Koch, K., 2013. Eight years of continuous quality assessment of the International Data Centre (IDC) reviewed event bulletin, *Bull. seism. Soc. Am.*, **103**(1), 296–305.
- Kværna, T. & Ringdal, F., 2013. Detection capability of the seismic network of the International Monitoring System for the Comprehensive Nuclear Test-Ban-Treaty, *Bull. seism. Soc. Am.*, **103**(2A), 759–772.
- Lazecký, M. *et al.*, 2020. LiCSAR: an Automatic InSAR Tool for measuring and monitoring tectonic and volcanic activity, *Remote Sens.*, **12**, doi:10.3390/rs12152430.
- Liu, F., Elliott, J., Craig, T., Hooper, A. & Wright, T., 2021. Improving the resolving power of InSAR for earthquakes using time series: a case study in Iran, *Geophys. Res. Lett.*, **48**, doi:10.1029/2021GL093043.
- Lohman, R. & Simons, M., 2005. Locations of selection small earthquakes in the Zagros mountains, *Geochem. Geophys. Geosyst.*, **6**, doi:10.1029/2004GC000849.
- Mellors, R.J., Magistrale, H., Earle, P. & Cogbill, A., 2004. Comparison of four moderate-size earthquakes in Southern California using seismology and InSAR, *Bull. seism. Soc. Am.*, **94**(6), 2004–2014.
- Myers, S.C., Johannesson, G. & Hanley, W., 2007. A Bayesian hierarchical method for multiple-event seismic location, *Geophys. J. Int.*, **171**(3), 1049–1063.
- Myers, S.C., Simmons, N.A., Johannesson, G. & Matzel, E., 2015. Improved regional and teleseismic P-wave travel-time prediction and event location using a global 3D velocity model, *Bull. seism. Soc. Am.*, **105**(3), 1642–1660.
- Ritz, J., Baize, S., Ferry, M., Larroque, C., Audin, L., Delouis, B. & Mathot, E., 2020. Surface rupture and shallow fault reactivation during the 2019 MW 4.9 Le Teil earthquake, France, *Commun. Earth Environ.*, **1**, doi:10.1038/s43247-020-0012-z.
- Rost, S. & Thomas, C., 2009. Improving seismic resolution through array processing techniques, *Surv. Geophys.*, **30**, 271–299.
- Simmons, N.A., Myers, S.C., Morency, C., Chiang, A. & Knapp, D.R., 2021. SPiRaL: a multiresolution global tomography model of seismic wave speeds and radial anisotropy variations in the crust and mantle, *Geophys. J. Int.*, **227**, 1366–1391.
- UN, 1998. *CTBT, Comprehensive Nuclear Test-Ban-Treaty*, United Nations, Dept. for Disarmament Affairs and Dept. of Public Information, New York, <https://www.ctbto.org/the-treaty/treaty-text/>.
- Wells, D. & Coppersmith, K., 1994. New empirical relationships among magnitude, rupture length, rupture width, rupture area, and surface displacement, *Bull. seism. Soc. Am.*, **84**, 974–2001.
- Wessel, P., Luis, J.F., Uieda, L., Scharroo, R., Wobbe, F., Smith, W.H.F. & Tian, D., 2019. The Generic Mapping Tools Version 6, *Geochem. Geophys. Geosyst.*, **20**(11), 5556–5564.
- Weston, J., Ferreira, A. & Funning, G., 2012. Systematic comparisons of earthquake source models determined using InSAR and seismic data, *Tectonophysics*, **532–535**, 61–81.

## SUPPORTING INFORMATION

Supplementary data are available at *GJI* online.

**Figure S1.** 10 coseismic interferograms, wrapped. Figure is the same as Fig. 5 in the main manuscript, but without unwrapping the interferograms.

**Figure S2.** Coherence plots for three coseismic interferograms, prior to spatial filtering.

Please note: Oxford University Press is not responsible for the content or functionality of any supporting materials supplied by the authors. Any queries (other than missing material) should be directed to the corresponding author for the paper.